Simulation of Oxy-Coal Combustion in a 100 kW$_{th}$ Test Facility Using RANS and LES: A Validation Study

Lei Chen[†] and Ahmed F. Ghoniem*[,†]

[†]Department of Mechanical Engineering, Massachusetts Institute of Technology, 77 Massachusetts Avenue, Cambridge, Massachusetts 02139-4307, United States

ABSTRACT: Oxy-fuel combustion of solid fuels, often performed in a mixture of oxygen and wet or dry recycled carbon dioxide, has gained significant interest in the last two decades as one of the leading carbon capture technologies in power generation. This paper presents a numerical study on oxy-fuel combustion of lignite coal in a 100 kW$_{th}$ test facility using Large-Eddy Simulation (LES) and Reynolds-averaged Navier−Stokes (RANS) approaches, along with radiation and char combustion submodels properly modified for the CO_2-rich environment. The performance of different turbulence models is investigated by comparing their predictions with experimental measurements of velocity and species concentrations as well as gas and particle temperatures. Results show that although agreeing reasonably with the measured mean axial and tangential velocity, all the RANS turbulence models used in this study underestimate the internal recirculation zone size and the turbulence mixing intensity in the char combustion zone. The standard $k−\varepsilon$ and RNG $k−\varepsilon$ models with default model constants fail to predict accurately the flow and mixing process associated with the staging stream and perform poorly on the oxygen concentration prediction. The SST $k−\omega$ model captures most of the flow regimes and improves the prediction of oxygen diffusion than other turbulent-viscosity models. LES can resolve some of the large-scale turbulent structures of the swirling flow in the burner quarl and of the staging stream downstream of the burner, better matching the measured internal recirculation zone size, the entrainment of oxygen from the staging stream, and the overall flame length than the RANS approaches. The unsteady LES approach captures the dynamic characteristics of oxy-coal combustion, such as the attached volatiles flame and the mixing between the recirculated hot gases and the unburned burner streams as well as the stable coal particle devolatilization and ignition in the quarl, which indicates good flame stability. The simulation shows that oxidation reactions dominate char consumption in oxy-fuel combustion. However, gasification reactions can be important locally in the fuel-rich zone of the volatiles-flame and the char-combustion regions, where the temperature is high and the oxygen concentration is low.

1. INTRODUCTION

Concerns over climate change have led to a growing effort to develop technologies for the reduction of carbon dioxide (CO_2) emissions from power plants, such as postcombustion, precombustion, and oxy-fuel combustion technologies.[1,2] Since the first time oxy-coal combustion was proposed with the objective of producing CO_2 for enhanced oil recovery (EOR) and for greenhouse gas reduction,[3] this technology has attracted growing interest. Previous studies have investigated the characteristics and fundamentals of oxy-fuel combustion in terms of the heat transfer, combustion kinetics, flame characteristics, and pollutant formations (see ref 4−8 for reviews). Moreover, oxy-coal combustion has been demonstrated at an industrial scale by Vattenfall in a 30 MW$_{th}$ plant.[5,9] Such activities have made considerable contributions to the development of this process. On the other hand, this new combustion environment raises challenges in modeling and simulations because of the high concentration of CO_2 and H_2O.[10] The high CO_2 partial pressure affects the thermodynamic, transport, and chemical properties of the reacting medium, the radiative heat transfer, and the oxy-char reaction mechanism, which should be considered in the modeling.

Turbulence is one of the most challenging and critical processes in turbulent combustion modeling, because of its role in establishing the flow, mixing, and combustion processes. RANS approaches, especially turbulent-viscosity models such as the $k−\varepsilon$ model, the $k−\omega$ model, and their variations,[11−14] are widely applied in the modeling of turbulent combustion because of their low computational cost. Specifically in oxy-coal combustion computational fluid dynamics (CFD) simulations, the standard $k−\varepsilon$ model has been extensively used.[15−22] For instance, Toporov et al.[19] chose the standard $k−\varepsilon$ model in their CFD modeling of the 100 kW$_{th}$ oxy-coal combustion test at Aachen University, and Al-Abbas et al.[22] used the same turbulence model to investigate air-fired and oxy-fuel coal combustion in a similar scale test facility at Chalmers University of Technology. CFD simulations of a full-scale (330 MW$_e$)[21] pulverized coal-fired furnace have also been conducted using the standard $k−\varepsilon$ model. Reasonably good agreements were observed when comparing the temperature and species distributions in these studies. However, the impact of turbulence models on the discrepancy between experimental and simulation results have not been fully assessed.

The $k−\varepsilon$ model has been shown to perform rather poorly in shear layers with strong pressure gradients, while the $k−\omega$ model performs better for many flows.[23] Based on a literature review on the performance of the RANS models in coal gasification, Kumar and Ghoniem[24,25] demonstrated that the shear-stress
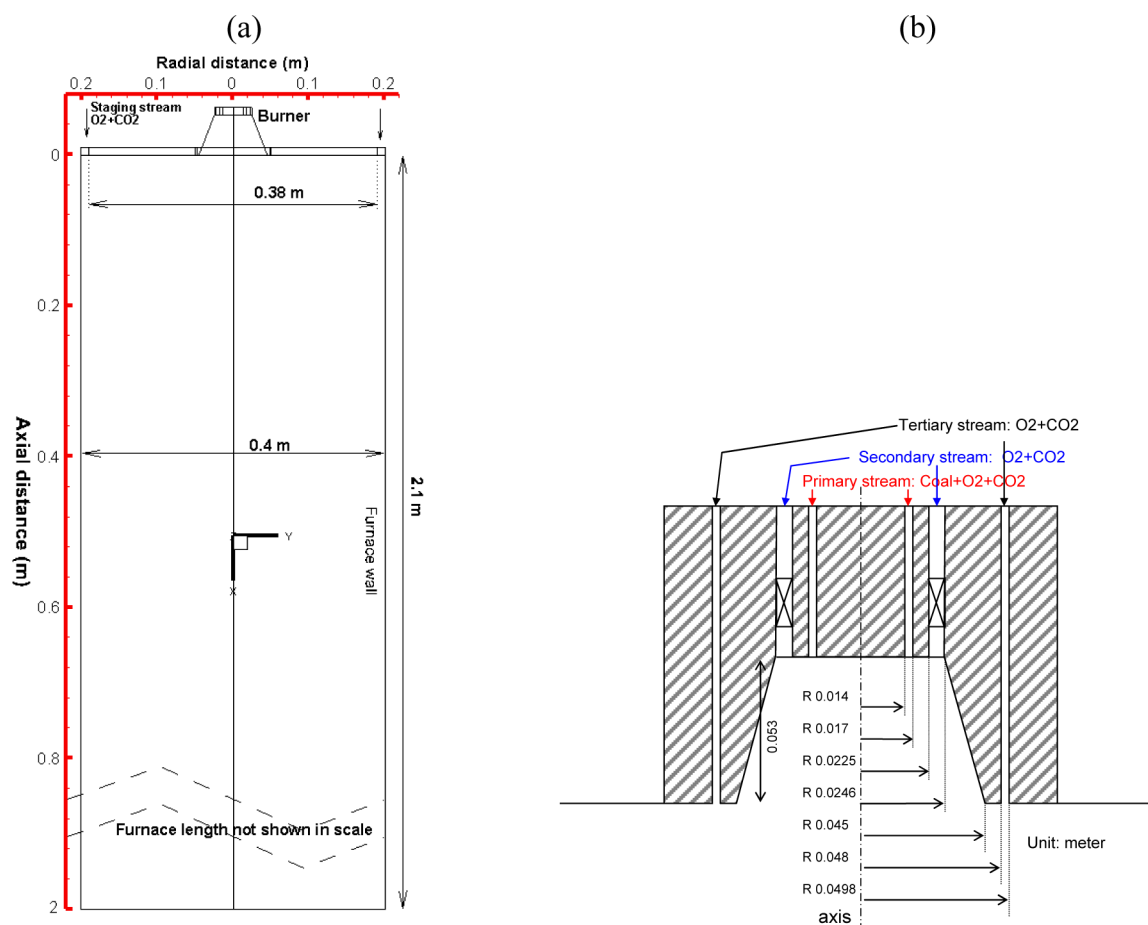
Figure 1. The geometry of (a) RWTH Aachen University 100 kW$_{th}$ test facility and (b) swirl burner, in meter. The mass flow rate, composition, and temperature of the burner streams are summarized in Table 1.

transport (SST) $k-\omega$ model performs better than the $k-\varepsilon$ models in swirling flows. They conducted simulation using the standard and the realizable $k-\varepsilon$ models, the SST $k-\omega$ model, and LES to predict the flow in a sudden expansion, and showed that the SST $k-\omega$ model yields the most satisfactory predictions among the RANS approaches in swirling and nonswirling canonical flow cases. We note here that although swirling flows are widely used in coal burner designs, there are few applications of the $k-\omega$ model in oxy-coal combustion simulations.

In recent years, LES has attracted more interest in CFD simulation. LES can capture the time-dependent large-scale flow dynamics and is less dependent on the assumed turbulence model. However, it is computationally more expensive. LES has been applied to model oxy-coal combustion, and results showed better agreement with experiments. For instance, Edge et al.[26] compared the performance of LES and RANS (renormalization-group (RNG) $k-\varepsilon$) models in their simulations of air-fired and oxy-fuel pulverized coal combustion in a 0.5 MW$_{th}$ test facility. Gharebaghi et al.[27] modeled a 1 MW$_{th}$ industrial test facility using LES and RANS (standard $k-\varepsilon$). Both studies suggest that LES improves the prediction of the recirculation zones and flame shape. It has also been realized that the radiation model needs to be modified in order to improve the prediction of the temperature field and the heat transfer characteristics.

In this study, both RANS (standard $k-\varepsilon$ model, RNG $k-\varepsilon$ model, SST $k-\omega$ model) and LES approaches, along with improved submodels for gas radiation properties and char

consumption in a CO_2-rich environment, are performed to investigate the oxy-fuel combustion of lignite coal in a pilot-scale test facility at RWTH Aachen University. Velocity, species concentration, gas and particle temperature measurements are used to examine the accuracy of the CFD simulations. In particular, the study focuses on assessing the performance of RANS turbulence models and LES approaches in a typical swirling flow burner equipped with multiple staging streams. Based on the simulation results, some of the mechanisms of oxy-combustion, such as the stabilization mechanism and the oxy-char combustion characteristics, are also discussed.

2. EXPERIMENTAL STUDIES

2.1. Furnace and Burner Geometry. The geometry and operating conditions of the oxy-lignite coal combustion experiments in a 100 kW$_{th}$ test facility[19,28] at the Institute of Heat and Mass Transfer of RWTH Aachen University was used in this numerical study. The axial and tangential mean velocities, averaged oxygen, and temperature distributions were measured at different locations downstream of the burner. These results are used to examine the accuracy of the CFD simulations. Figure 1(a) shows the geometry of the cylindrical furnace. The length of the combustion chamber is 2.1 m, and its inner diameter is 0.4 m. The burner shown in Figure 1(b) is a swirl burner with an annular orifice through which the primary stream is supplied with coal particles. The secondary stream is swirled with a velocity ratio $(v_{tan})/(v_{axial}) = 1$, and it is injected into the combustion chamber through an annulus surrounding the primary stream inlet. According to a geometry-based correlation for the vane-type swirler in an axial tube proposed by Beer and Chigier,[29] the swirl number of the secondary
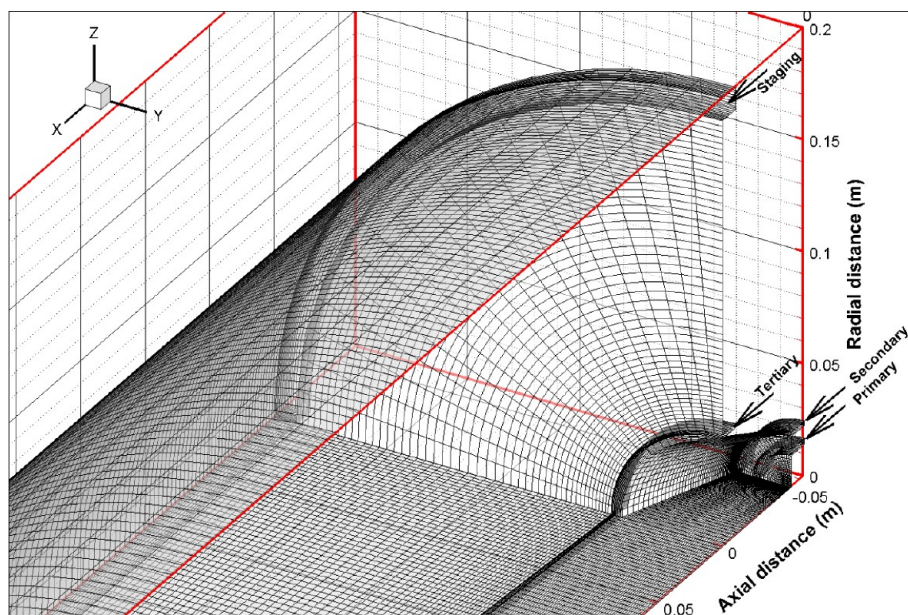
Figure 2. The three-dimensional mesh for Aachen' 100 kW$_{th}$ oxyfuel combustion test facility. The figure shows only the part in the vicinity of the burner.

stream is close to 0.96. A more accurate calculation using the CFD simulation results shows that the swirl number of the secondary stream is 1.06, which takes the pressure gradient into account. Moreover, the CFD calculated swirl number at the burner quarl outlet is 0.81 combining the nonswirled primary and the swirled secondary streamflow. A tertiary stream can be injected through an annulus enclosing the quarl. Another gas stream, the staging fluid, enters the furnace through an annulus at the outer diameter of the furnace. Its main purpose is to reduce the amount of gas injected through the other inlet openings, thus reducing the axial velocities and maintaining local fuel-rich stoichiometry at the burner.

Based on the burner and the furnace geometry, a three-dimensional mesh was generated for one quadrant taking advantage of the axisymmetric character of the furnace and burner. Figure 2 shows part of the mesh where local refinement was used to improve the resolution near the burner. The mesh consists of 383,420 cells, and only hexahedron cells are used in order to minimize numerical diffusion. A mesh-independent study was performed by comparing the RANS simulation results with those obtained from a finer two-dimensional axisymmetric mesh consisting of 24,000 quadrangular cells and those from another three-dimensional mesh consisting of 590,800 cells. The differences of the predicted velocity and species concentrations between these meshes were negligible.

2.2. Operating Conditions and Measurement Techniques. In the Aachen University oxyfuel combustion experiment, the oxidizer mixture was provided by a gas mixing unit instead of flue gas recycle. The compositions and mass flow rates of the four streams are shown in Table 1. The overall oxygen/fuel ratio described by the stoichiometry value (oxygen/fuel)/(oxygen/fuel)$_{st}$ was 1.3, while the local stoichiometry at the burner (with oxygen provided by primary, secondary, and tertiary streams only) was set to 0.6, the remaining

Table 1. Operating Conditions of the Oxy-Coal Combustion Experiment at RWTH Aachen University

	mass flow rate (kg/h)	O$_2$ content (vol%)	CO$_2$ content (vol%)	temperature (°C)
coal	6.5			
primary stream	17.6	19	81	40
secondary stream	26.6	21	79	60
tertiary stream	1.5	21	79	60
staging stream	54.9	21	79	900

Table 2. Proximate and Ultimate Analysis of the Rhenish Lignite Used in the Experiments

	as received	dry	DAF
proximate analysis (wt%)			
water	8.40		
ash	4.10	4.48	
volatiles	46.60	50.87	53.26
char	40.90	44.65	46.74
ultimate analysis (wt%)			
water	8.40		
ash	4.10	4.48	
carbon	67.40	73.58	77.03
hydrogen	4.24	4.63	4.85
oxygen	14.70	16.05	16.80
nitrogen	0.86	0.94	0.98
sulfur	0.30	0.33	0.34

oxidizer mixture was injected through the staging stream. A predried Rhenish lignite coal was used in the experiment, and its properties are shown in Table 2. The experimentally tested particle size distribution (PSD) of the pulverized lignite coal is shown in Figure 3. This PSD is represented using 6400 particles with a size range of 5−100 μm in the CFD simulations. The 6400 particles follow a Rosin-Rammler distribution with a mean diameter of 35.2 μm and spread parameter of 1.218, that are least-square regressed from the experimental measurement.

Multiple techniques were used in order to measure the velocity, gas and particle temperature as well as the gas composition during the experiments. Laser Doppler anemometry (LDA) was applied for the nonintrusive measurements of the axial and tangential velocities. Coal and ash particles in the coal flame were used as tracers, with the assumption that the slip velocity between the particles and the gas was negligible for the small coal particles used in the experiment ($D_{p90} <$ 75 μm). Gas samples were collected using a water-cooled suction probe with a ceramic tip, and the concentration of oxygen was measured by a magnetomechanical analyzer. The gas temperature was measured using a PtRh/Pt thermocouple mounted within a ceramic tip (D_{outer} = 27 mm) of a water-cooled stainless steel traversable suction probe, while the particle temperature was measured by a two-color pyrometer. The reader is referred to ref 19 for more detail on the measurement techniques and processes.
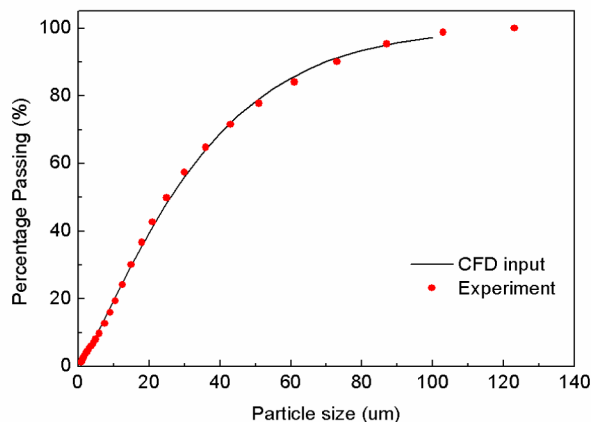
Figure 3. The particle size distribution of the coal used in experiment and CFD simulations.

3. MODELING APPROACHES

This section briefly introduces the approaches and submodels used in the CFD simulations, including the turbulence submodels in RANS and LES and the combustion models for coal and gas phase reactions as well as the modified submodels for radiative heat transfer.

3.1. Modeling Turbulence: RANS Simulation. In variable-density problems such as compressible flows and reacting flows, the Favre-averaged Navier−Stokes equations are solved. Taking density weighted time average of the instantaneous continuity and momentum equations, we obtain the Favre-averaged Navier−Stokes equations as

$$\frac{\partial \overline{\rho}}{\partial t} + \frac{\partial}{\partial x_i}(\overline{\rho}\,\tilde{u}_i) = 0 \tag{1}$$

$$\frac{\partial}{\partial t}(\overline{\rho}\,\tilde{u}_i) + \frac{\partial}{\partial x_j}(\overline{\rho}\,\tilde{u}_i\tilde{u}_j)$$
$$= -\frac{\partial \overline{p}}{\partial x_i} + \frac{\partial}{\partial x_j}\left[\mu\left(\frac{\partial \tilde{u}_i}{\partial x_j} + \frac{\partial \tilde{u}_j}{\partial x_i} - \frac{2}{3}\delta_{ij}\frac{\partial \tilde{u}_k}{\partial x_k}\right)\right]$$
$$+ \frac{\partial}{\partial x_j}(-\overline{\rho u_i' u_j'}) \tag{2}$$

where $\tilde{u}_i$, $\tilde{u}_j$, and $\tilde{u}_k$ are the Favre-averaged velocity components, and u_i' and u_j' are their fluctuations in the Cartesian coordinate, $\overline{\rho}$ and $\overline{p}$ are the standard time-averaged density and statistic pressure, and μ is the molecular viscosity of the fluid.

The Reynolds stresses $-\overline{\rho u_i' u_i'}$ are unknown. In turbulent-viscosity models, such as the $k-\varepsilon$ and the $k-\omega$ model, the Reynolds stresses are related to the mean velocity gradients and turbulent viscosity, μ_t, using the Boussinesq hypothesis

$$-\overline{\rho u_i' u_j'} \approx \mu_t\left(\frac{\partial \tilde{u}_i}{\partial x_j} + \frac{\partial \tilde{u}_j}{\partial x_i} - \frac{2}{3}\delta_{ij}\frac{\partial \tilde{u}_k}{\partial x_k}\right) - \frac{2}{3}\overline{\rho}k\delta_{ij} \tag{3}$$

In the standard $k-\varepsilon$ model,[11] the turbulent viscosity, μ_t, is modeled as a function of the turbulent kinetic energy, k, and its dissipation rate, ε

$$\mu_t = \overline{\rho}\,C_\mu\frac{k^2}{\varepsilon} \tag{4}$$

which are obtained by solving two transport equations

$$\frac{\partial}{\partial t}(\overline{\rho}k) + \frac{\partial}{\partial x_i}(\overline{\rho}k\tilde{u}_i)$$
$$= \frac{\partial}{\partial x_j}\left[\left(\mu + \frac{\mu_t}{\sigma_k}\right)\frac{\partial k}{\partial x_j}\right] + G_k + G_b - \rho\varepsilon - Y_M \tag{5}$$

$$\frac{\partial}{\partial t}(\overline{\rho}\varepsilon) + \frac{\partial}{\partial x_i}(\overline{\rho}\varepsilon\tilde{u}_i)$$
$$= \frac{\partial}{\partial x_j}\left[\left(\mu + \frac{\mu_t}{\sigma_\varepsilon}\right)\frac{\partial \varepsilon}{\partial x_j}\right] + C_{1\varepsilon}\frac{\varepsilon}{k}(G_k + C_{3\varepsilon}G_b) - C_{2\varepsilon}\overline{\rho}\frac{\varepsilon^2}{k} \tag{6}$$

where G_k and G_b are the generation of turbulence kinetic energy due to the mean velocity gradients and buoyancy, respectively; Y_M represents the contribution of the fluctuating dilatation in compressible turbulence to the overall dissipation rate; σ_k and σ_ε are the turbulent Prandtl numbers for k and ε; $C_{1\varepsilon}$, $C_{2\varepsilon}$, $C_{3\varepsilon}$, C_μ, σ_k, and σ_ε are default model constants. The RNG $k-\varepsilon$ model[12] has a similar transport equation form for k and ε, but it includes the effect of swirl on turbulence.

In the $k-\omega$ model,[13] the turbulent viscosity is computed as a function of k and the specific dissipation rate $\omega \equiv \varepsilon/k$

$$\mu_t = \alpha^*\frac{\overline{\rho}k}{\omega} \tag{7}$$

and again k and ω are obtained from two transport equations

$$\frac{\partial}{\partial t}(\overline{\rho}k) + \frac{\partial}{\partial x_i}(\overline{\rho}k\tilde{u}_i) = \frac{\partial}{\partial x_j}\left[\left(\mu + \frac{\mu_t}{\sigma_k}\right)\frac{\partial k}{\partial x_j}\right] + G_k - Y_k \tag{8}$$

$$\frac{\partial}{\partial t}(\overline{\rho}\omega) + \frac{\partial}{\partial x_i}(\overline{\rho}\omega\tilde{u}_i) = \frac{\partial}{\partial x_j}\left[\left(\mu + \frac{\mu_t}{\sigma_\omega}\right)\frac{\partial \omega}{\partial x_j}\right] + G_\omega - Y_\omega \tag{9}$$

where α^* is the damping coefficient for turbulent viscosity, G_k and G_ω are the generation of k and ω, while Y_k and Y_ω represent the dissipation of k and ω due to turbulences. The SST $k-\omega$ model[14] retains the $k-\omega$ model formulation in the near-wall region and switches to the standard $k-\varepsilon$ model in the far field region using an appropriate blending function and a "cross-diffusion" term. The modification makes the SST model more accurate in adverse pressure gradient flows and swirling flows.[24]

3.2. Modeling Turbulence: Large Eddy Simulation. Different from the RANS approach in which turbulence is modeled at all scales, in LES, the time-dependent Navier−Stokes equations are filtered in physical or wavenumber space. Therefore, in principle, the large eddies that transport most of the momentum, mass, and energy are directly resolved, while the small subgrid-scale eddies that dissipate energy are modeled.[30] A filtered variable is defined by

$$\overline{\phi}(x) = \int_D \phi(x')G(x, x')dx' \tag{10}$$

where D is the fluid domain, and G is the filter function that determines the scale of the resolved eddies. The filter function is applied in the finite-volume discretization scheme

$$G(x, x') = \begin{cases} 1/V, & x' \in \nu \\ 0, & x' \notin \nu \end{cases} \tag{11}$$

where ν is the computational cell, and V is the volume of the cell. The filtered variable becomes

$$\bar{\phi}(x) = \frac{1}{V} \int_\nu \phi(x') dx', \quad x' \in \nu \tag{12}$$

The Favre-filtered Navier−Stokes equations are

$$\frac{\partial \bar{\rho}}{\partial t} + \frac{\partial}{\partial x_i}(\bar{\rho}\,\tilde{u}_i) = 0 \tag{13}$$

$$\frac{\partial}{\partial t}(\bar{\rho}\,\tilde{u}_i) + \frac{\partial}{\partial x_j}(\bar{\rho}\,\tilde{u}_i\tilde{u}_j)$$
$$= -\frac{\partial \bar{p}}{\partial x_i} + \frac{\partial}{\partial x_j}\left[\mu\left(\frac{\partial \tilde{u}_i}{\partial x_j} + \frac{\partial \tilde{u}_j}{\partial x_i} - \frac{2}{3}\delta_{ij}\frac{\partial \tilde{u}_k}{\partial x_k}\right)\right] - \frac{\partial \tilde{\tau}_{ij}}{\partial x_j} \tag{14}$$

The over bar and tilde in the variables represent standard-filtered and Favre-filtered value, respectively. The subgrid-scale stress, $\tilde{\tau}_{ij}$, is defined by

$$\tilde{\tau}_{ij} \equiv \bar{\rho}\left(\widetilde{u_i u_j} - \tilde{u}_i\tilde{u}_j\right) \tag{15}$$

Similar to the RANS model, the subgrid-scale turbulent stresses are assumed to have the form

$$\tilde{\tau}_{ij} = \frac{1}{3}\tilde{\tau}_{kk}\delta_{ij} - 2\mu_t\hat{S}_{ij} \tag{16}$$

where $\tilde{\tau}_{kk}$ is the isotropic part of the subgrid-scale stresses, and $\hat{S}_{ij}$ is the rate-of-strain tensor for the resolved scale defined by

$$\hat{S}_{ij} \equiv \frac{1}{2}\left(\frac{\partial \tilde{u}_i}{\partial x_j} + \frac{\partial \tilde{u}_j}{\partial x_i}\right) \tag{17}$$

The subgrid-scale turbulent viscosity μ_t is modeled using the Smagorinsky-Lilly model,[31] in which the eddy-viscosity is computed from

$$\mu_t = \bar{\rho}L_s^2|\hat{S}| \tag{18}$$

where $|\hat{S}| \equiv (2\hat{S}_{ij}\hat{S}_{ij})^{1/2}$, and L_s is the mixing length for subgrid scales calculated from

$$L_s = \min(\kappa d, C_s\Delta) \tag{19}$$

where κ is the von Kármán constant, d is the distance to the closest wall, C_s is the Smagorinsky constant, and Δ is the local grid scale defined as $V^{1/3}$.[30] It is also assumed that the centroid of the wall-adjacent cell falls within the logarithmic region of the boundary layer, and the law-of-the-wall is employed as the near-wall treatment.

Since the LES approach resolves the evolution of the large scale eddies, it is believed to be more accurate. However, it requires refined time and space discretization and involves significantly higher computational cost.

3.3. Coal Combustion Submodels. Pulverized coal combustion is modeled as a dilute two-phase (solid−gas) reacting flow using an Eulerian-Lagrangian approach. The mass, momentum, and energy interactions between the gas phase and the solid particles are calculated using the "particle-source-in-cell" method[32] while updating the particle state along a set of particle trajectories. In total, 6400 particle representing 20 sizes between 5 and 100 μm were tracked in the simulations starting at the primary stream inlet of the burner. No apparent changes can be observed when the number of tracked particles was doubled or halved. The particle size follows the Rosin-Rammler distribution shown in Figure 3.

3.3.1. Modeling Coal Devolatilization. The single kinetic rate devolatilization model was used to describe the thermal decomposition rate of dry coal particles

$$-\frac{dm_p}{dt} = k[m_p - (1 - f_{v,0})(1 - f_{w,0})m_{p,0}] \tag{20}$$

where m_p and $m_{p,0}$ are the current and initial particle mass, $f_{v,0}$ is the mass fraction of volatiles on a dry basis, and $f_{w,0}$ is the mass fraction of moisture initially present in the coal particle as received, respectively. The rate constant, k, is given by

$$k = Ae^{-(E/R_u T_p)} \tag{21}$$

where $R_u = 8314$ J/(kmol·K) is the ideal gas constant, and T_p is the particle temperature. Since the devolatilization kinetics data for this lignite coal are not provided in the experimental study, kinetics parameters were taken from the literature. The activation energy, E, was taken from Badzioch and Hawksley[33] ($E = 4.64e7$ J/kmol), and the pre-exponential factor, A, was taken to be 20,000 as suggested by Al-Abbas et al.[22]

3.3.2. Modeling Oxy-Char Combustion. Char combustion in a CO_2 rich environment has been investigated in recent years. Bejarano and Levendis[34] and Shaddix and Molina[35] found that, when the oxygen concentrations in the gas are the same, the char burning temperatures are lower, and burnout times are longer under O_2/CO_2 conditions than in O_2/N_2. Using a detailed single particle combustion model, Shaddix and co-workers discussed the effect of CO_2 on oxy-char combustion and attributed the differences to CO_2's distinct physical properties, such as the diffusivity and volumetric heat capacity, as well as the char-CO_2 and char-H_2O gasification reactions.[36,37] The different physical properties and chemical effects of CO_2 should be considered when modeling oxy-char burning process in CFD simulations.

In conventional air-fired combustion, the Single-Film Model (SFM) is appropriate for the burning of char with typical pulverized coal particle sizes. Mitchell et al.[38] modeled the CO oxidation process in the coal particle boundary layer and suggested that little CO_2 is formed in the boundary layer when the char diameter is smaller than 100 μm. For oxy-fuel combustion, Chen et al.[8] showed that the SFM along with appropriate diffusivity can capture the trends of lower char temperature and reaction rates in oxy-char combustion. Hecht et al.[37] found that the SFM is adequate for the simulation of a 130 μm diameter particle burning when oxygen mole fraction is below 12%. These facts warrant the applicability of SFM for the size range of pulverized coal combustion in the present study.

On the other hand, gasification reactions may play a role in determining the char particle temperature and burning rate. The char-CO_2 gasification reaction may enhance the overall char consumption rate for oxygen concentrations up to 24%, while it reduces the overall consumption rate in environments with greater than 24% oxygen due to the endothermicity of the gasification reaction.[37] In this study, three heterogeneous reactions are considered on the char external surface

$$2C(s) + O_2 \rightarrow 2CO \tag{22}$$

$$C(s) + CO_2 \rightarrow 2CO \tag{23}$$

$$C(s) + H_2O \rightarrow CO + H_2 \tag{24}$$

In the oxidation reaction (eq 22), only CO is considered as the combustion product, which diffuses away from the char surface and reacts with oxygen to form carbon dioxide in the computational cell. This assumption is valid because the CO_2/CO ratio formed by the heterogeneous reaction on the char surface is less than 0.1 at normal combustion temperatures.[39]

The char reaction rate, $\dot{m}_{p,i}$, by heterogeneous reaction i depends on the external diffusion rate, D_i, and the surface reaction kinetic rate, R_i

$$\dot{m}_{p,i} = -A_p p_i \frac{D_i R_i}{D_i + R_i} \tag{25}$$

where A_p is the external surface area of the char particle, p_i is the partial pressure of species i in the bulk gas. The kinetic rate of the char external surface reactions, R_i, is represented in an Arrhenius form

$$R_i = A_i T_p^{\beta_i} \exp\left[\frac{-E_i}{R_u T_p}\right] \tag{26}$$

where the kinetics parameters were taken from empirical data for low-rank coal char in refs 19, 40, and 41. Diffusion often controls the char-O_2 reaction rate at high temperatures. Following the approach described in ref 42, the mass transfer limited reaction rate, D_i, can be expressed as

$$D_i = C_i \frac{[(T_p + T_\infty)/2]^{0.75}}{d_p} \tag{27}$$

where T_∞ is the gas temperature in the cell, and d_p is the particle diameter. C_i is the mass diffusion limited constant expressed as a function of the binary diffusivity and heterogeneous reaction stoichiometric coefficients as well as the operating pressure[8]

$$C_i = \nu_i MW_c \cdot \frac{1}{R_u T_0^{1.75}} \cdot Sh \cdot DF_{i,0} \frac{P_0}{P} \tag{28}$$

where ν_i is the stoichiometric coefficient of carbon relative to the gas phase reactant i in the oxidation and gasification reactions (eqs 22-24); MW_c is the molecular weights of carbon. T_0 and P_0 are the reference temperature and pressure for the binary diffusivity $DF_{i,0}$. P is the operating pressure of the furnace. R_u is the gas constant, and Sh is the Sherwood number. The oxy-char submodel is implemented into the CFD code in the form of a User Defined Function (UDF). The parameters and coefficients used for the heterogeneous reactions are listed in Table 3.

Table 3. Kinetics Parameters and Diffusion Coefficients for the Oxy-Char Surface Reactions

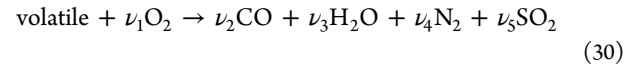| reaction	A_i $kg/(m^2sPa)$	E_i kJ/mol	β_i	C_i $s/K^{0.75}$	ref
eq 22	0.005	74	0	4.41×10^{-12}	19,58
eq 23	0.00635	162	0	2.47×10^{-12}	19,41
eq 24	0.00192	147	0	2.47×10^{-12}	

3.4. Modeling Gas Phase Reaction. In the flame zone, gas phase reactions are mostly limited by the extent of mixing,

because the turbulent mixing rate is generally slower than the kinetic rate. The eddy dissipation model (EDM)[43,44] was used in this study, in which the chemical reaction is governed by the large-eddy mixing time scale, k/ε, proposed by Spalding.[44] Based on the assumption that the reaction rate is limited by both the mixing of the reactants and the heating of the reactants through the mixing with the products, the net rate of production of species i due to reaction r, $R_{i,r}$, is given by the smaller of the reactant mixing rate (first term) and product mixing rate (second term)

$$R_{i,r} = \min\left(\begin{array}{c} \nu'_{i,r} M_{w,i} A \rho \dfrac{\varepsilon}{k} \min_R\left(\dfrac{Y_R}{\nu'_{R,r} M_{w,R}}\right), \\[3mm] \nu'_{i,r} M_{w,i} A B \rho \dfrac{\varepsilon}{k} \dfrac{\sum_P Y_P}{\sum_j^N \nu''_{j,r} M_{w,j}} \end{array}\right) \tag{29}$$

where $\nu'_{i,r}$ and $\nu''_{j,r}$ are the stoichiometric coefficient for reactant i and product j in reaction r, M_w is the molecular weight, and Y_R and Y_P are mass fraction of any reactant and product species, respectively. $A = 4.0$ and $B = 0.5$ are empirical model constants.

Three gas phase reactions were considered

$$\text{volatile} + \nu_1 O_2 \rightarrow \nu_2 CO + \nu_3 H_2O + \nu_4 N_2 + \nu_5 SO_2 \tag{30}$$

$$CO + 0.5O_2 \rightarrow CO_2 \tag{31}$$

$$H_2 + 0.5O_2 \rightarrow H_2O \tag{32}$$

taking the burning of volatiles, carbon monoxide, and hydrogen into account. The coefficients ν_i in reaction 30 are calculated using the coal proximate and ultimate analysis data in Table 2 according to mass and element balance. It should be noted that the EDM does not incorporate finite rate kinetics. Therefore, this model can only be used to predict the major products species for stable diffusion flames in which the reaction rates are controlled by turbulent mixing. Since the simplified gas phase reaction scheme in reactions 30−32 could not reflect the chemical effect of CO_2 on hydrocarbon oxidation,[45,46] it should not be expected to show accurate prediction of intermediate species such as CO and H_2 in oxy-fuel combustion. Validation of the reaction mechanisms for oxy-fuel combustion remains a subject of investigation.

3.5. Modeling Radiative Heat Transfer in Oxy-Fuel Combustion. Radiation dominates the heat transfer in the combustion environment, especially within the flame zone, and it is modeled by solving the radiative transfer equation (RTE). The RTE at position $\vec{r}$ in the direction $\vec{s}$ takes the form[47]

$$\frac{dI_\lambda(\vec{r}, \vec{s})}{ds} = \kappa_\lambda n^2 I_{b,\lambda} - (\kappa_\lambda + \sigma_{s,\lambda}) I_\lambda(\vec{r}, \vec{s})$$
$$+ \frac{\sigma_{s,\lambda}}{4\pi} \int_0^{4\pi} I_\lambda(\vec{r}, \vec{s}') \Phi(\vec{s} \cdot \vec{s}') d\Omega' \tag{33}$$

where s is the path length, κ is the absorption coefficient, σ_s is the scattering coefficient, n is the refractive index, and $I_\lambda(\vec{r}, \vec{s})$ is the spectral radiation intensity which is dependent on position $\vec{r}$ and direction $\vec{s}$.

Thermal radiation is directional in the wavenumber space. In this study, the Discrete Ordinates (DO) model[48,49] is used to solve the RTE. Each octant of the angular space 4π is discretized into 3×3 solid angles, and a total of 72 RTE equations are solved

in the three-dimensional space. It is computationally expensive to solve radiative heat transfer in each wavelength band, and gray gas models such as the weighted-sum-of-gray-gas model (WSGGM)[50] are used to calculate the absorption coefficient of the participating gas mixture. In WSGGM, the absorption coefficient of the gas mixture is assumed to be the weighted-average of several (3 or 4) gray gases and a transparent gas; therefore, it is a function of the H_2O and CO_2 concentrations and gas temperature. The model coefficients are derived from experimental data for oil and methane stoichiometric combustion, in which the CO_2 partial pressure is around 0.1 atm, and the partial pressure ratio of H_2O and CO_2 is in the range of 1 to 2, with a path length of less than 10 m.[51] However, it is worth noting that the CO_2 and H_2O partial pressures and their relative ratio in oxy-coal combustion are not within the applicable range. Johansson et al.[52] modified the coefficients of the three gray-one clear gases model by fitting the emissivity to a Statistical Narrow Band (SNB) model. The new parameters are applicable under oxy-fuel conditions with dry or wet flue gas recycle in the temperature range of 500−2500 K and for path lengths between 0.01 and 60 m. Similar to the method in ref 53, the modified WSGGM was implemented in the CFD simulation in the form of UDF. In the modified three gray-one clear WSGGM, the Planck-mean absorption coefficient of the gas mixture over a path length, s, is determined by

$$\overline{a} = -\ln(1 - \varepsilon)/s \tag{34}$$

where s is the radiation beam length, and ε, the gas emissivity. The former is estimated to be ∼0.6 m based on an average dimension of the furnace domain; while the latter is calculated from

$$\varepsilon = \sum_i a_{\varepsilon,i}(T)(1 - \exp(-\kappa_i p_i s)) \tag{35}$$

where $a_{\varepsilon,i}$ is the emissivity weighting factor for gray gas i, κ_i and p_i are the pressure absorption coefficient $(1/(\text{pa·m}))$ and partial pressure (Pa) of the absorbing gas i, respectively. The emissivity weight factors $a_{\varepsilon,i}$ used in the previous eq 35 are polynomial correlations which are given as a function of the gas temperature

$$a_{\varepsilon,i} = \sum_j b_{\varepsilon,i,j}\left(\frac{T}{T_{ref}}\right)^{j-1} \tag{36}$$

where $T_{ref} = 1200$ K is a reference temperature. The coefficients of the polynomial correlations, $b_{\varepsilon,i,j}$, and the pressure absorption coefficients of the gray gas, κ_i, are summarized in Table 4.

Table 4. Coefficients Used in the Three Gray-One Clear Gases WSGG Model for Oxy-Fuel Combustion, Adapted from Ref 52

gray gas i	$\kappa_i \times 10^5 \left(\frac{1}{\text{Pa·m}}\right)$	$b_{\varepsilon,i,1}$	$b_{\varepsilon,i,2}$	$b_{\varepsilon,i,3}$
1	0.0992	0.4995	−0.0170	−0.0393
2	2.6589	0.3418	−0.1701	0.0196
3	88.1078	0.1273	−0.0726	0.0101

Moreover, the contribution of the particles (coal, char, and ash) to the radiative heat transfer is also considered by modeling its absorption and scattering coefficient in the RTE.

3.6. Boundary Conditions. Mass flow rate boundary conditions are used for the burner inlets, i.e., the primary, secondary, tertiary, and staging streams. The pressure outlet boundary condition is used at the furnace outlets. Measured wall temperatures are used for all the thermal boundary conditions in the simulation. Temperature ($T_{wall} = 1000$ °C) and heat flux ($q'' = 0$) thermal boundary conditions are used for the furnace wall and burner surfaces, respectively, with emissivity of 0.7 and 0.2 as suggested in the experimental study.[22]

3.6. Solution Strategy. FLUENT 12.1 was used as the computation platform for this CFD study. For the RANS simulation, the three-dimensional pressure-based solver with double precision was chosen to solve the steady-state governing equations. Second-order upwind scheme is used for the momentum, species transport, energy, and radiation equations. A converged solution was obtained for the cold flowfield with species transport after about 5000 iteration steps, and the Lagrangian tracking of coal particles, gas phase reactions, and radiative heat transfer submodels were added to the system of equations. Converged solutions for the reacting flow were obtained after about 50,000 iteration steps. The RANS simulations were performed on the Pharos computing cluster of MIT, using 8 parallel AMD Magny-Cours 12-core 2.2 GHz processor cores. It takes about 90 h clock time for each of the RANS simulation until convergence is achieved.

In the LES, a second-order bounded central differencing scheme is applied to solve the momentum equation, and second-order upwind scheme is used for the species transport, energy, and radiation equations. The time dependent terms are discretized using a second-order implicit scheme with an initial time step of 0.2×10^{-4} second, such a value guarantees that the Courant number is smaller than 1 in most of the computational cells. After obtaining a stable combustion field, the time step was increased to 1×10^{-4} second progressively. The LES starts with the converged RANS reacting flow solutions, and the unsteady calculation takes about 4−5 flow residence times, or about 1.5 s flow-time, to achieve fully developed reacting flow. The time-averaged statistics were obtained with another 0.5 s flow-time simulation. In general, for unsteady simulation of 1 s flow time, it takes about 300 h clock time using 32 parallel processor cores on the same computing cluster.

4. RESULTS AND DISCUSSIONS

In this section, the CFD predictions are compared with the measurements in the test facility, especially in the vicinity of the burner where oxygen and fuel particle mix and the volatiles flame is stabilized. In particular, the performance of the different RANS turbulence models and the LES are compared, and their impacts on the mixing and reaction processes are discussed.

4.1. Velocity Field. Figure 4 shows a comparison between the experimental measurements and the CFD simulations for the axial and tangential velocity profiles. In general, RANS and LES results capture the overall trends of the flowfield. However, they perform differently in terms of predicting the internal recirculation zone size and the mixing intensity between the burner streams and the staging stream. From Figure 4(a), it can be seen that all the turbulence models show an internal recirculation zone along the centerline downstream of the burner outlet, a positive axial velocity peak of 6−9 m/s at around 0.05 m in the radial direction, and an external recirculation zone at around 0.07−0.15 m in the radial direction. The swirling secondary burner stream is responsible for establishing the internal recirculation zone, along with the bluffbody and quarl geometries. Another axial velocity peak is observed near the outer diameter of the furnace where the staging stream is injected. In Figure 4(b), all the simulation models show that the peak
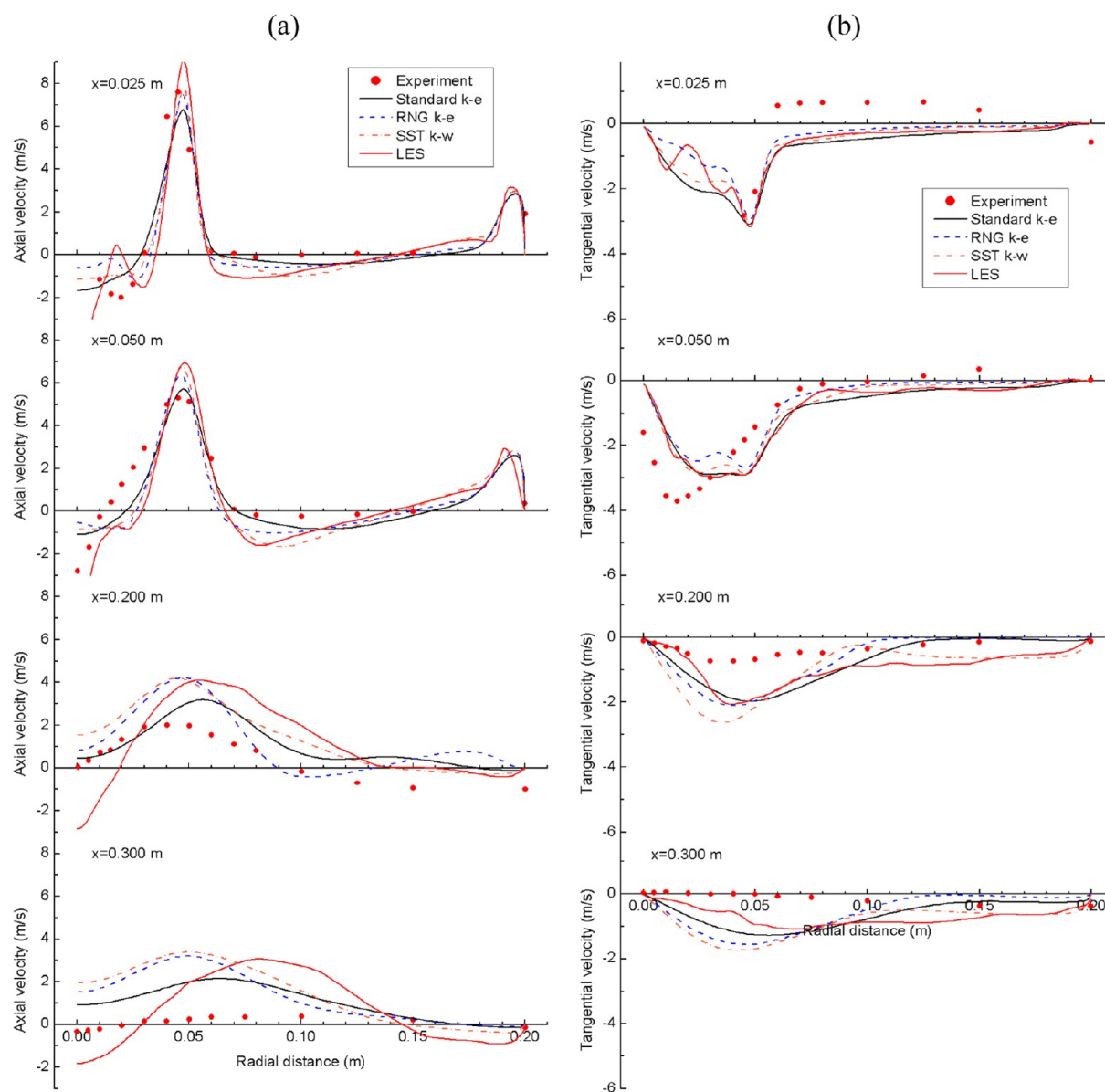
Figure 4. Comparison between the measured (scatters) and predicted (lines) velocity profiles at 0.025, 0.05, 0.2, and 0.3 m away from the burner outlet: (a) axial velocity and (b) tangential velocity.
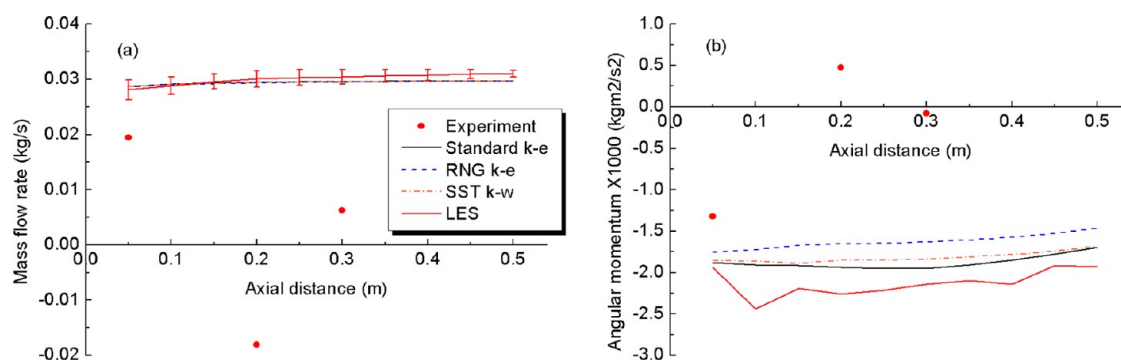

Figure 5. Comparison between the measured (scatters) and predicted (lines) gas phase mass flow rate and angular momentum along the axis: (a) mass flow rate in (kg/s) and (b) angular momentum in (kg m^2/s^2). The error bar with the LES results shows the velocity and density covariance term in mass flow rate calculation.

tangential velocity is reached at the burner outlet, and this peak decays in both the axial and radial directions.

Discrepancies between the simulation and the measured results are found downstream, at 0.2 and 0.3 m away from the
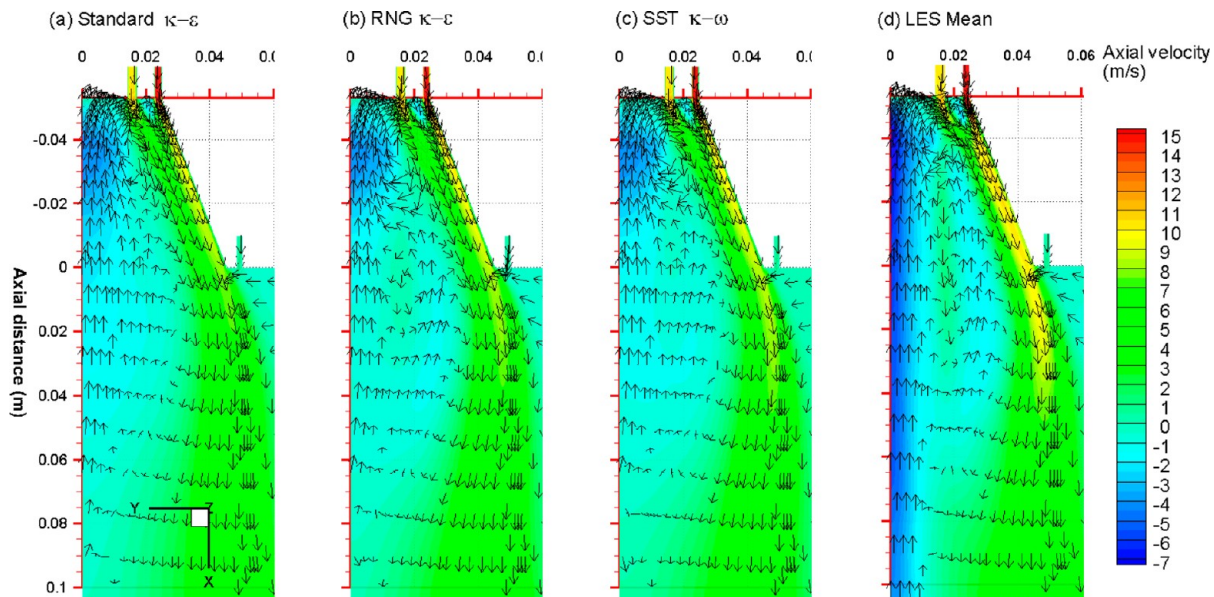
Figure 6. The predicted velocity distribution in the burner quarl using uniform vector length, colored by axial velocity. The results from (a) the standard $k-\varepsilon$ model, (b) the RNG $k-\varepsilon$ model, (c) the SST $k-\omega$ model, and (d) LES mean values show different internal recirculation zone sizes and peak reverse velocity.

burner exit. The simulation results show higher axial and tangential velocity magnitudes than the experimental results. In order to identify a possible source of the discrepancy, we calculated the total gas mass flow rate and the total angular momentum in the experimental and simulation results. Figure 5 shows the measured and CFD calculated average gas phase mass flow rate, $\bar{m}$, and angular momentum, $\bar{G}_{\phi}$. For the experimental results, these quantities are calculated as

$$\bar{m} = \int_0^R 2\pi r\bar{\rho}\,\bar{u}\,dr \tag{37}$$

$$\bar{G}_{\varphi} = \int_0^R 2\pi r\bar{\rho}\,\bar{u}\,(\bar{w}r)\,dr \tag{38}$$

where $\bar{u}$ and $\bar{w}$ are the measured mean axial and tangential velocity, respectively. Piecewise-polynomial representations of $\bar{u}$ and $\bar{w}$ were obtained by curve-fitting the measured mean velocity profiles in Figure 4. The gas density $\bar{\rho}$ is calculated using the measured mean gas temperature profiles (in Figure 11) and the ideal gas state equation. The measured $\bar{m}$ and $\bar{G}_{\phi}$ were calculated by substituting the piecewise-polynomial curves and integrating eqs 37 and 38 at different axial locations. Similarly, the mass flow rate and angular momentum can also be integrated at different cross sections along the axis using the simulation results. We note that the mean mass flow rate contains a density-velocity covariance term due to turbulence

$$\bar{m} = \int_0^R 2\pi r\bar{\rho}\,\bar{u}\,dr + \int_0^R 2\pi r\overline{\rho'u'}\,dr \tag{39}$$

which is omitted in eq 37. The magnitude of this covariance term was estimated using the LES results and shown in Figure 5. It is negligible compared to the first term because of the stable combustion dynamics.

The comparison in Figure 5 indicates several points:

- Figure 5(a) shows that the measured mass flow rate downstream is significantly lower than the total burner mass flow rate, which is 0.028 kg/s. The measured mass flow rate at x = 0.2 m is negative, which indicates that the

measured positive velocity in the inner radial section was lower, or the measured negative velocity in the external recirculation section (0.1 m < R < 0.2 m) was higher than the actual value. On the other hand, the simulation solution satisfies gas phase mass conservation as well as the mass exchange from coal particle (combustibles) to the flue gas.

- Figure 5(b) shows that the measured angular momentum decays faster than the predicted results.

The low measured axial and tangential velocities in the downstream sections may be partially due to the fact that coal/char particles were used as trace particles in the experimental measurement. We also note that the measured tangential velocity at the axis 0.05 m away from the burner shows a nonzero value. According to the experimental study, this might be due to "the minor misalignment between the burner and the furnace axes, or the procedure for alignment of the optical axis of the LDA system with the burner axis".[19]

Although all the simulations show the same overall trends, the turbulence models perform differently with regard to the near-burner internal recirculation zone and its peak velocities and the external recirculation zone.

- The internal recirculation zone: At 0.05 m away from the burner, LES reproduces the reverse velocity of about −3 m/s near the centerline (see Figure 4(a)), while the RANS simulations underestimate the peak reverse velocity. The experimental results at 0.3 m show that a reverse flow remains at the centerline, and only the LES can show this trend. It should be noted that the measured centerline axial velocity at x = 0.2 m is inconsistent with the measurements upstream and downstream. As mentioned previously, the velocity profile at this cross section does not conserve the mass flow rate. Figure 6 shows the internal recirculation zones predicted by the different turbulence models. Again, all RANS models underestimate the internal recirculation zone size, while a significantly longer recirculation zone with higher reverse velocities is predicted by the LES. As a result, more hot gases are recirculated back to mix with the
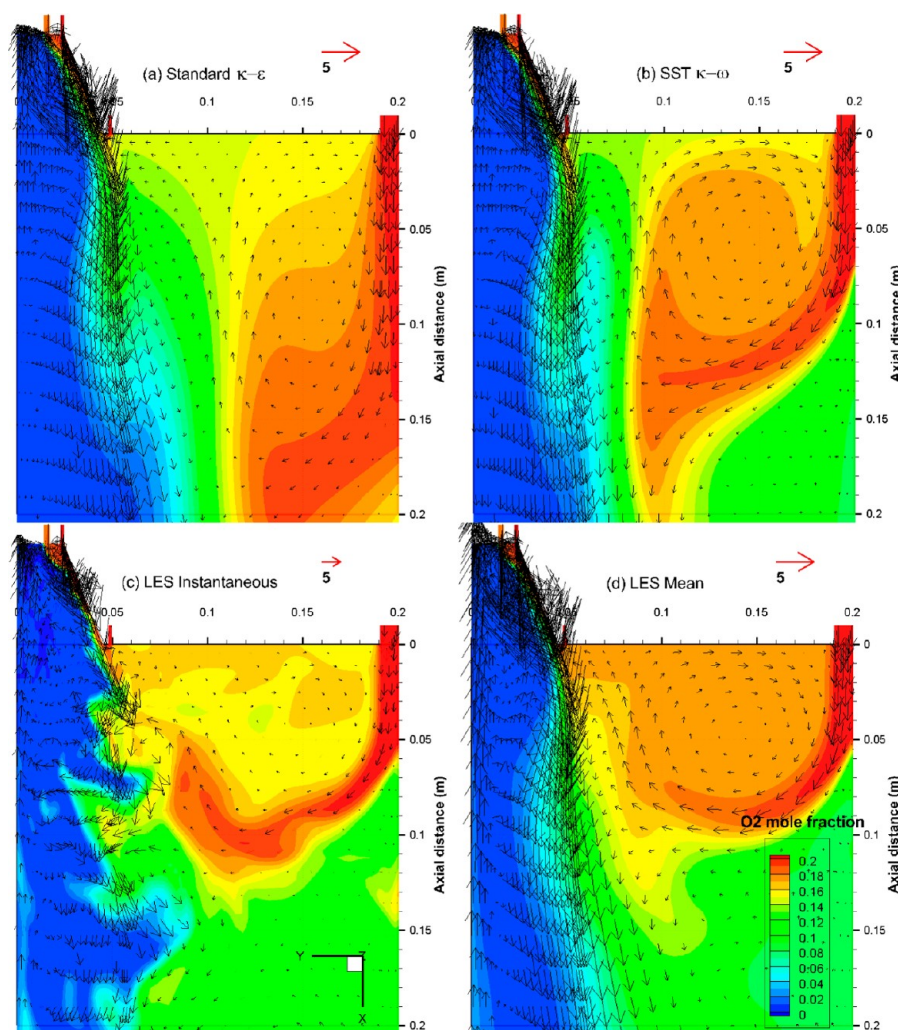
Figure 7. RANS and LES predicted velocity (scaled vector) and oxygen concentration (colored contour) distribution in the near-burner region, showing the mixing between the staging stream and the burner streams. The figures show the results from (a) the standard $k-\varepsilon$ model, (b) the SST $k-\omega$ model, (c) LES in an instantaneous moment, and (d) LES mean values. Note that the LES instantaneous velocity vector scale is different from others because the instantaneous velocity magnitudes are larger than the mean values.

unburned burner stream and stabilize the coal flame in the quarl, which results in a higher turbulent mixing between the burner streams and the staging stream as will be shown later.

- The external recirculation zone: At x = 0.2 m and x = 0.3 m, the measured axial velocity shows negative values (see Figure 4(a)), indicating an external recirculation zone. Only the SST $k-\omega$ model and LES predict the external recirculation zone. This external recirculation zone is induced by the strong entrainment of the staging stream, and it has an impact on the oxygen distribution, which will be discussed in the next section.

In general, the best match with the experimental results in terms of the velocity profiles is obtained using LES. Although the RNG $k-\varepsilon$ model accounts for the swirl effect in the turbulence viscosity calculation, it shows similar trends as those of the standard $k-\varepsilon$ model. The SST $k-\omega$ captures the external recirculation zone almost as close as the LES does, and it performs the best among the RANS models.

4.2. Mixing and Oxygen Diffusion. The radial velocity profiles were not reported in the experimental study. These are, however, critical to the mixing between the burner streams and the staging stream. Figure 7 shows the predicted velocity and oxygen concentration distributions in the vicinity of the burner using the standard $k-\varepsilon$ model, the SST $k-\omega$ model, and LES. For the latter, both instantaneous results and time-averaged values are shown. The RNG $k-\varepsilon$ model results are similar to those obtained using the standard $k-\varepsilon$ model; therefore, it is not shown here. As discussed previously, an internal recirculation zone is predicted by both the RANS and LES approaches. However, significant differences can be observed in the entrainment of the staging stream and its mixing with the burner streams. In the standard and RNG $k-\varepsilon$ models (see Figure 7(a)), the staging stream flows parallel to the burner streams, while the SST $k-\omega$ model (see Figure 7(b)) predicts a different flow: the staging stream separates from the wall, forming a wall recirculation zone which results in a better mixing with the burner streams. The unsteady LES simulation (see Figure 7(c)) shows more detail regarding the turbulent structure and shear layer at the burner exit, where the staging stream is entrained into and mixes with the fuel-rich stream. In all the tested RANS turbulence models, only the SST $k-\omega$ model shows this mixing process as that observed in the LES time-averaged results (see Figure 7(d)).
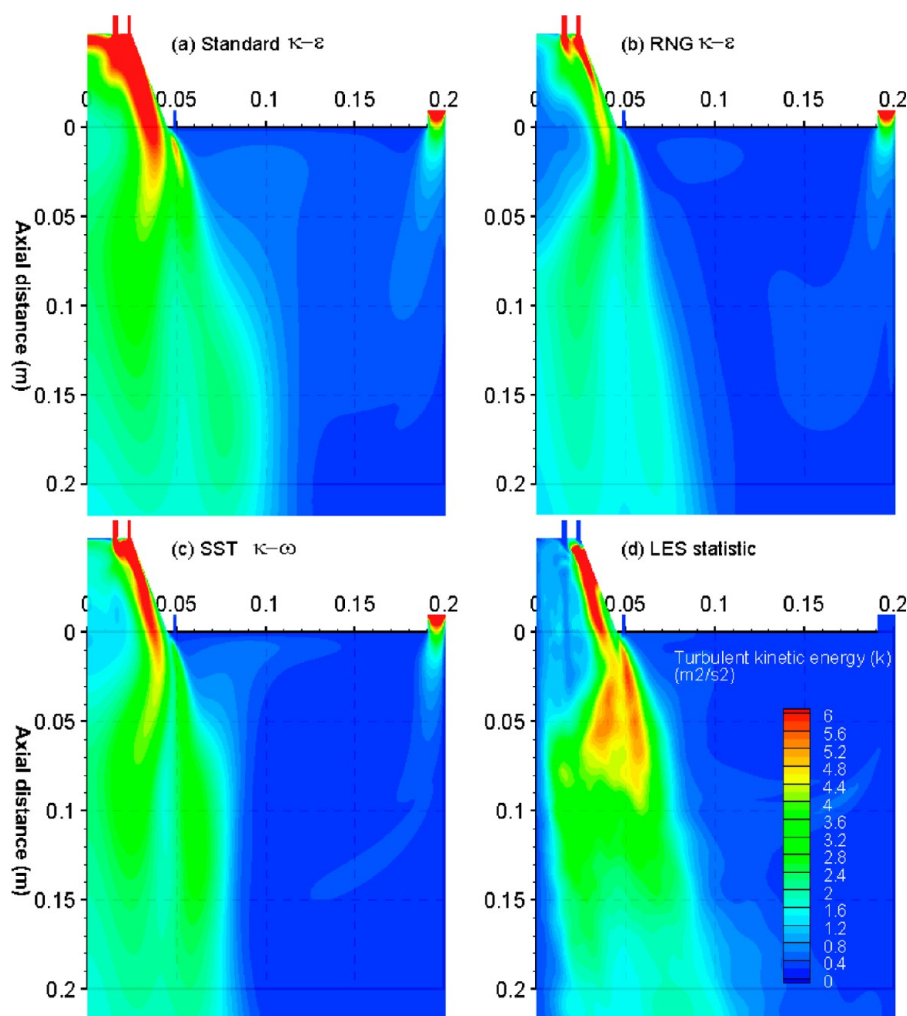
Figure 8. The predicted turbulent kinetic energy k in the near-burner region. The figures show the results from (a) the standard $k-\varepsilon$ model, (b) the RNG $k-\varepsilon$ model, (c) the SST $k-\omega$ model, and (d) LES statistic values.

Besides the mean velocity predictions, the other important quantity in turbulent flows is the velocity fluctuation, because of its role in mixing. Figure 8 compares the turbulent kinetic energy k predicted by the RANS and LES approaches. The turbulent kinetic energy is the mean kinetic energy per unit mass associated with the unsteadiness or the eddies in turbulent flow. It is defined as the square of the root-mean-square velocity fluctuations in three dimensions

$$k = \frac{1}{2}\left(\overline{u_i'^2} + \overline{u_j'^2} + \overline{u_k'^2}\right) \tag{40}$$

As discussed in section 3.1 and 3.2, in the RANS approaches, k is modeled using a transport equation; while in LES, the time dependent velocity is explicitly resolved, and k is calculated using the statistic results. Although all turbulence models show similar mean velocity profiles, they perform differently in predicting the turbulence intensity. The turbulent kinetic energy predicted by the LES approach is marginally higher than those predicted by the RANS models in the burner exit region, indicating more intense turbulence and better mixing between the staging stream and the burner streams.

Figure 9 shows the oxygen mole fraction profiles at 0.05, 0.1, 0.2, 0.3, and 0.5 m away from the burner. As a result of the different predicted flowfield and mixing processes, significantly different oxygen mole fraction distributions are observed when applying different turbulence models. For instance, the oxygen concentrations in the standard and RNG $k-\varepsilon$ model deviate from the measured results significantly in the outer radial section, especially at 0.2 and 0.3 m away from the burner. The same results have also been reported in previous numerical studies using the standard $k-\varepsilon$ model.[19,53] The RNG $k-\varepsilon$ model predictions agree poorly with the measured results, since it underpredicts the turbulent intensity in this region, as shown in Figure 8. On the other hand, the SST $k-\omega$ model and LES show a better match in these regions as they better predict the flowfield and the mixing process. Both the experimental and simulation results show low oxygen concentration near the axis and higher oxygen mole fraction in the outer region. Recalling that the stoichiometry in the burner region is set to 0.6, low oxygen mole fraction near the axis should be expected in the fuel-rich zone. The remaining oxygen is supplied by the staging stream for char burning in the downstream and that will be discussed in greater detail later.

In summary, we show that although similar mean axial and tangential velocity profiles are predicted by all the turbulence models, the standard and the RNG $k-\varepsilon$ model fail to predict the burner streams turbulence intensity and its mixing with the staging stream in the burner exit region, thus underestimating the downstream oxygen diffusion process. To the contrary, the SST $k-\omega$ model and LES can capture the formation of the
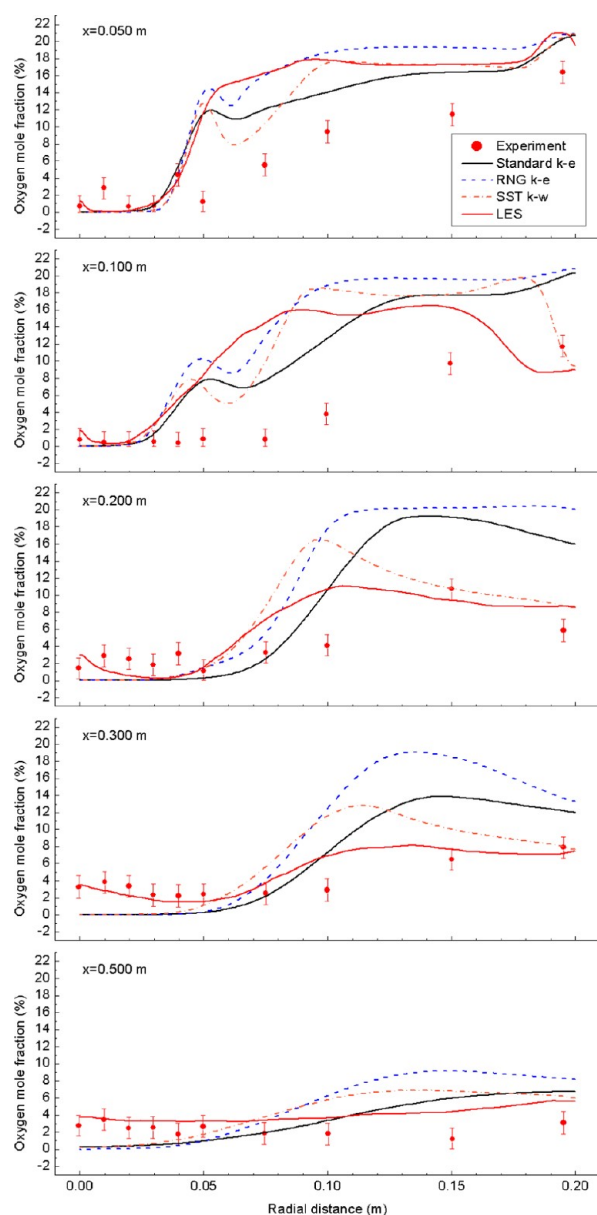
Figure 9. Comparison between the measured (scatters) and predicted (lines) oxygen mole fraction at 0.05, 0.1, 0.2, 0.3, and 0.5 m away from the burner. The error bar of the experimental results indicates two standard deviations.

recirculation zones induced by the staging stream and hence show a better match with the experimental results.

4.3. Temperature Distribution. Figure 10 compares the predicted temperature distribution in the furnace using the standard $k-\varepsilon$ model, the SST $k-\omega$ model, and LES. The results show similar trends but different flame lengths. The standard and RNG $k-\varepsilon$ models show longer flames because they underestimate the mixing of the staging stream. Although the SST $k-\omega$ model captures most of the average flow structures, it still underestimates the turbulent intensities as discussed previously. Intense mixing and temperature fluctuations in the char combustion zone are illustrated in the LES instantaneous result in Figure 10 (c). The LES time-averaged results match the experimental observations best in terms of the flame length, which can be seen more clearly in the comparison between the simulation and experimental results in Figure 11.
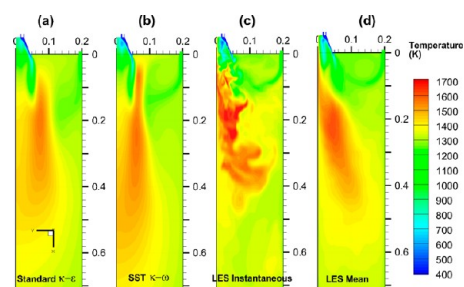

Figure 10. The predicted temperature distributions using RANS and LES: (a) the standard $k-\varepsilon$ model, (b) the SST $k-\omega$ model, (c) LES in an instantaneous moment, and (d) LES mean values.
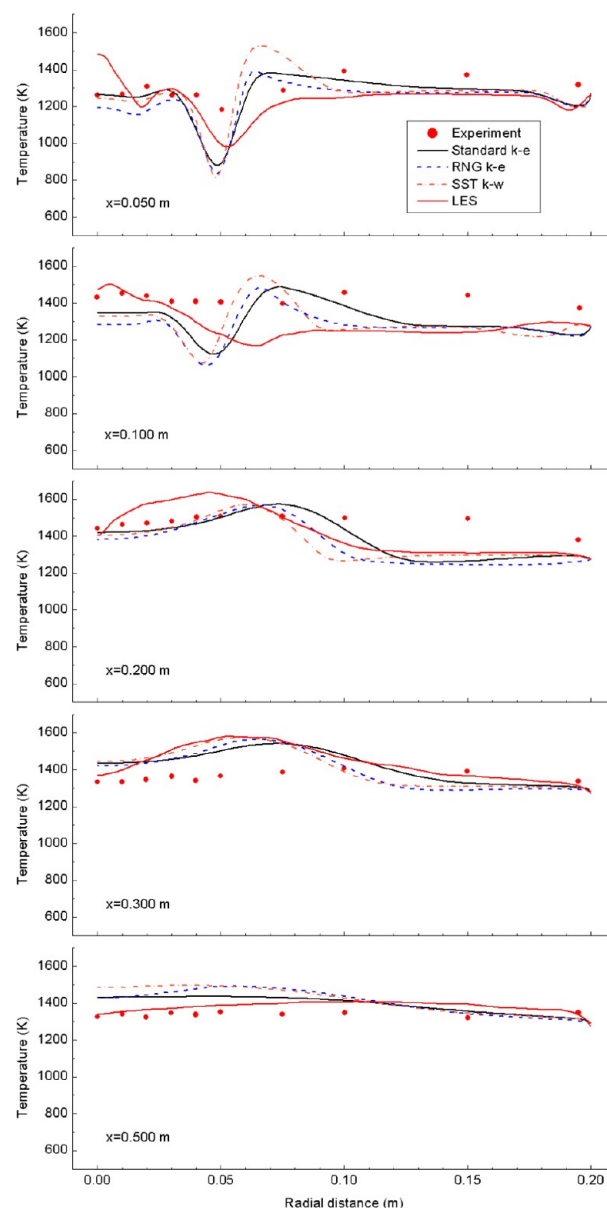

Figure 11. Comparison between the measured (scatters) and predicted (lines) gas temperature at 0.05, 0.1, 0.2, 0.3, and 0.5 m away from the burner.

Although predicting apparently different flowfield, the three RANS turbulence models predict similar temperature profiles in the furnace, while LES performs marginally better. For instance,
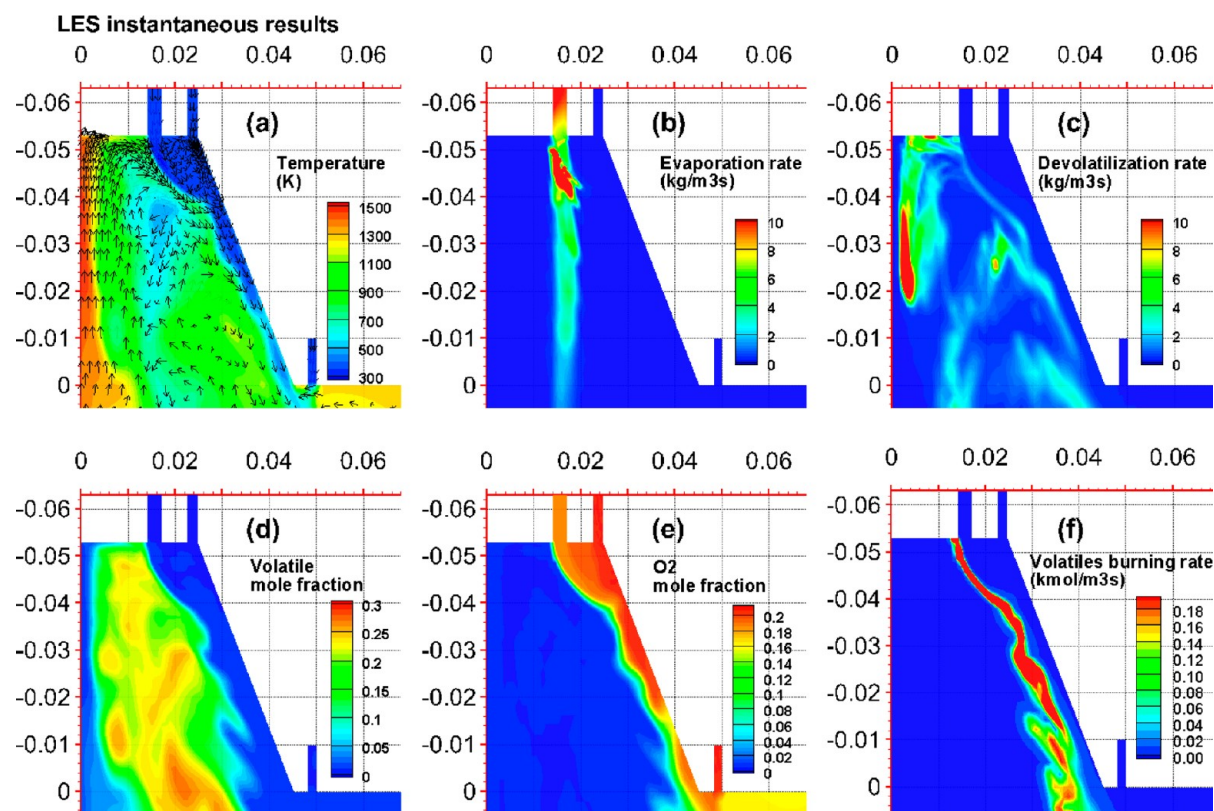
Figure 12. The LES instantaneous results, showing the flame stabilization mechanism in the burner quarl. (a) Gas temperature is shown using colored contour, and velocity is shown using uniform length vector, (b) coal particle moisture evaporation rate, (c) coal particle devolatilization rate, (d) volatiles mole fraction, (e) O_2 mole fraction, and (f) volatiles burning rate in the quarl structure.

at 50 mm away from the burner, the predicted gas temperature by all the turbulence models closely follows the experimental results. However, in RANS, the minimum temperature at 0.05 m off axis is 300 K lower than the measured data, likely to be due to the burner cold stream penetration, while LES show a marginally improved result. This is because the RANS models underestimate the turbulent mixing between the staging stream and the burner streams. A similar trend has been reported by Gharebaghi et al.[27] who compared the temperature predictions by the standard $k-\varepsilon$ model and LES in an industrial coal combustion facility: they found that the RANS simulation was not able to predict the turbulence structures downstream the burner, leading to a longer and narrower flame than that predicted by LES and observed in the experiment. LES shows better temperature predictions at 0.05 ma and 0.1 m away from the burner, indicating that it models the turbulent mixing and reaction rates in the burner downstream more accurately. This is also shown at x = 0.5 m where the LES results match the temperature measurements, while the RANS approaches overestimate the flame length.

All the simulation underestimated the gas temperature in the outer radial region (0.1 m < R < 0.2 m) at 0.1 and 0.2 m away from the burner: the predicted gas temperatures are about 200 K lower than the measured results. Recalling that all simulations overpredict the oxygen concentration in the same location, this might be partially due to the gas phase reaction model, the assumed coal devolatilization and char combustion kinetic parameters, or the deviation on particle trajectory predictions. The discrepancy may also be partially due to the experimental errors. Note that the diameter of the suction pyrometer tip is ~1/8 of the furnace radius, which may disturb the flowfield and average out the radial profiles.

4.4. Flame Stabilization and Oxy-Char Combustion.
The CFD provides some insight into the coal combustion process, in particular the volatile flame stabilized in the vicinity of the burner, and the oxy-char combustion downstream.

Flame destabilization has been reported in oxy-coal combustion due to the different thermodynamic and transport properties.[54] Maintaining flame stability and keeping the heat transfer characteristics in oxy-fuel combustion similar to those in air combustion may be achieved by adjusting the flue gas recycle ratio,[55] partitioning of the gas volume and oxygen contents in different burner streams,[56,57] as well as using advanced burner design. The swirl burner used in the test facility was specifically designed for oxy-coal combustion with low oxygen concentrations and has demonstrated favorable aerodynamics features in the experiment.[28] Using unsteady LES simulation, the flame stabilization mechanism can be revealed. Combustion in this case is characterized by an attached flame, sufficient mixing between the recirculated hot gas and unburned burner streams, and stable coal particle devolatilization and ignition. Figure 12(a) shows the gas temperature and velocity distribution in the burner quarl. A stream of hot gas up to 1500 K is recirculated to the primary and secondary stream inlets along the centerline, which maintains the high temperature in the burner quarl. Figure 12(b) shows the coal dewatering processes: because of the fine particle size used in the experiment, the evaporation process takes place early in the primary stream duct, and nearly all the particles are dried out as soon as they are injected into the high temperature zone. Figure 12(c) shows the volatile release rate in the quarl: coal particles start releasing volatiles following the dewatering process, some of the coal particles are recirculated back following the gas flow while continuing the devolatilization process. Figure 12(d) and
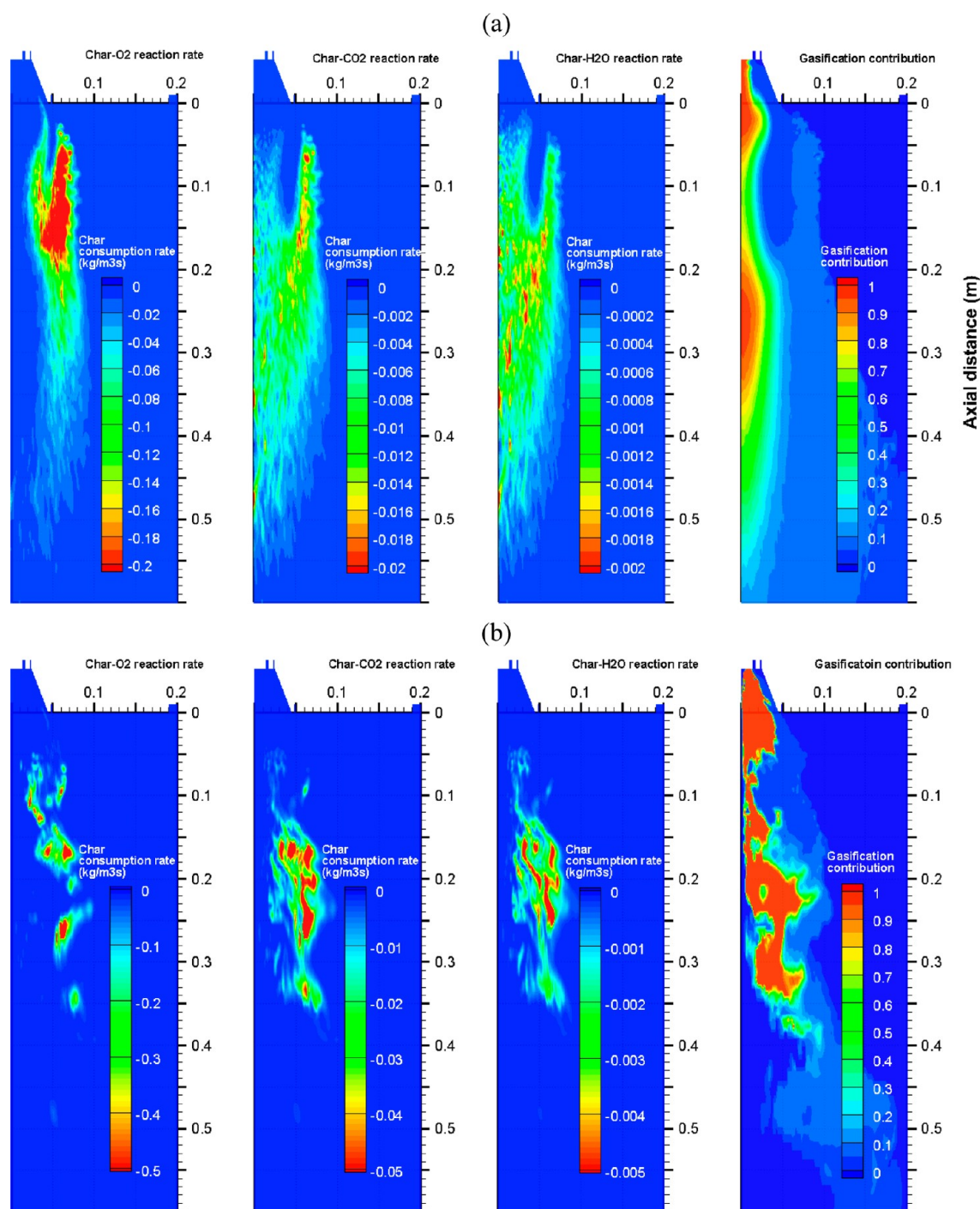
Figure 13. Predicted char consumption rate by oxidation and gasification reactions and the gasification reaction's contribution: (a) the SST $k-\omega$ model and (b) LES in an instantaneous moment.

(e) shows the volatile and oxygen concentration distributions in the quarl. A volatile mole fraction up to 30% shows that volatile matters are concentrated in the recirculation zone. Figure 12(f) shows the volatiles burning rate (reaction in eq 30). The volatiles are burned by the oxygen supplied from the primary and secondary streams. The wrinkled interface between the volatile and oxygen streams shows that a turbulent diffusion flame is stabilized near the burner quarl wall, which agrees well with the experimental observations.

Following volatiles combustion, char particles are burned further downstream using mostly the oxygen supplied from the

staging stream. Figure 13 shows the char consumption rates due to the char oxidation and gasification reactions predicted by the SST $k-\omega$ model and the instantaneous result predicted by LES. Following the trajectory of the coal particles, char is burned using the oxygen supplied by the stating stream at the burner outlet where intense mixing takes place due to the local turbulence, as discussed in section 4.2. The char-O_2 reaction occurs mainly within 0.3 m away from the burner, in accordance with the experimental observations.[19] On the other hand, the char-CO_2 and char-H_2O gasification reactions can be observed across a broader region. However, noting the different contour ranges

used in the figures, the gasification reaction rates are one to 2 orders of magnitude lower than the oxidation reaction because of their higher activation energies. In oxy-fuel combustion, char consumption is dominated by the oxidation reactions because of their higher reaction rates. The contributions of the char-O_2, char-CO_2, and char-H_2O reactions to char consumption are 91.9%, 7.46%, and 0.68%, respectively. However, the gasification reactions may become important locally where the gas temperature is high and the oxygen concentration is low.[8] As shown in the last chart of Figure 13(a) and (b), the gasification reactions' contribution reaches up to 90% in the fuel-rich zone of the volatile-flame and the char-combustion regions, where the gas temperature is high and oxygen concentration is low. It should be noted that, because the calculations are based on a simplified oxy-char combustion model and global reaction kinetics, the relative contributions of oxidation and gasification reactions are only qualitative. They may vary depending on the coal rank, burner designs, and operating conditions such as overall stoichiometry and dry or wet flue gas recycle as well as the flue gas recycle ratio.

The experimental study also measured the particle temperature distribution at several axial locations. Figure 14 shows a
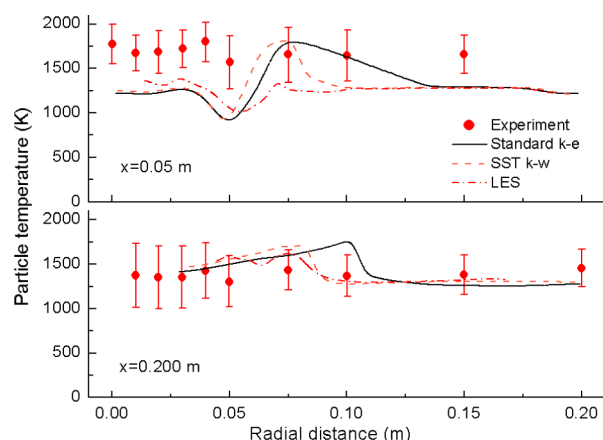

Figure 14. Comparison between the measured (scatters) and CFD predicted (lines) particle temperature at 50 and 200 mm away from the burner.

comparison between the measurement and the CFD simulations. It should be noted that the two-color pyrometry method used in the experiment is based on optical measurement of the infrared radiation intensity of the hot coal particle at two selected wavelengths, and only particles which are hotter than the background gas are detected. The same criteria were used when the particles were sampled in the CFD analysis. Figure 14 shows that the computed particle temperature follows the same trends as those observed in the experiment. However, the simulation results are significantly lower than the measured particle temperature at 0.05 m away from the burner, showing less burning intensity in a mean statistical sense, while the simulation results at 0.2 m away from the burner match the experimental results well. This may be due to the fact that only few char particles are burned at 0.05 m (see Figure 13), where the experimental result might have a higher uncertainty because hotter particles can be detected with higher probability.

5. CONCLUSION

In this paper, three-dimensional CFD simulations were performed for oxy-fuel lignite coal combustion in a 100 kW$_{\text{th}}$

pilot-scale combustion unit using RANS and LES approaches as well as radiation and char-combustion submodels modified specifically for a high CO_2 concentration oxy-combustion environment. The predicted velocity, species, and temperature distributions using different turbulence models, such as the standard $k-\varepsilon$ model, the RNG $k-\varepsilon$ model, the SST $k-\omega$ model, and LES model, were compared with experimental results. These turbulence models show different performance in predicting the turbulent flowfield, which significantly impacts the prediction of oxygen diffusion, coal combustion, and temperature distribution. The main conclusions are as follows:

(1) All turbulence models show the overall trends of the measured mean axial and tangential velocity profiles and capture the internal and external recirculation zone formed by the swirling burner stream. However, the RANS models underestimate the internal recirculation zone size and the turbulent intensity at the burner exit. LES shows better performance in predicting the turbulent structure and flowfield and matches well with the experiment.

(2) The different performance of these turbulence models leads to different oxygen concentration predictions: the standard $k-\varepsilon$ model and the RNG $k-\varepsilon$ model fail to predict the entrainment and mixing of the staging stream, while the SST $k-\omega$ model can capture the corresponding flow structures and improve the oxygen concentration prediction. Nevertheless all the RANS models underestimate the turbulence intensity downstream in the char combustion zone, while LES shows intense mixing and oxygen diffusion, which also improves the prediction of the flame length and temperature field.

(3) LES provides insights into the flame stabilization mechanism. The swirling flow forms strong internal recirculation zone along with the bluffbody and quarl geometry, which stabilizes the volatiles diffusion flame in the quarl.

(4) Char-O_2 reaction contributes up to 91.9% of the char consumption and dominates the char combustion process in oxy-fuel combustion. However, gasification reactions can become important locally at the fuel-rich zone of the volatile-flame and char-combustion regions, where the gas temperature is high and oxygen concentration is low.

■ AUTHOR INFORMATION

Corresponding Author
*Phone: +1 617 253 2295. Fax: +1 617 253 5981. E-mail: ghoniem@mit.edu.

Notes
The authors declare no competing financial interest.

■ REFERENCES

(1) IPCC Contribution of Working Groups I, II and III to the Fourth Assessment Report of the Intergovernmental Panel on Climate Change; Intergovernmental Panel on Climate Change: 2007.

(2) Ghoniem, A. F. *Prog. Energy Combust. Sci.* **2011**, 37 (1), 15−51.

(3) Abraham, B.; Asbury, J.; Lynch, E.; Teotia, A. *Oil Gas J.* **1982**, *80* (11), 68−70.

(4) Buhre, B. J. P.; Elliott, L. K.; Sheng, C. D.; Gupta, R. P.; Wall, T. F. *Prog. Energy Combust. Sci.* **2005**, *31* (4), 283−307.

(5) Wall, T.; Liu, Y.; Spero, C.; Elliott, L.; Khare, S.; Rathnam, R.; Zeenathal, F.; Moghtaderi, B.; Buhre, B.; Sheng, C.; Gupta, R.; Yamada, T.; Makino, K.; Yu, J. *Chem. Eng. Res. Des.* **2009**, *87* (8), 1003−1016.

(6) Toftegaard, M. B.; Brix, J.; Jensen, P. A.; Glarborg, P.; Jensen, A. D. *Prog. Energy Combust. Sci.* **2010**, *36*, 581−625.

(7) Zheng, L. *Oxy-fuel combustion for power generation and carbon dioxide (CO₂) capture*; Woodhead Publishing Limited: Philadelphia, 2011.

(8) Chen, L.; Yong, S. Z.; Ghoniem, A. F. *Prog. Energy Combust. Sci.* **2012**, *38* (2), 156−214.

(9) Strömberg, L.; Lindgren, G.; Jacoby, J.; Giering, R.; Anheden, M.; Burchhardt, U.; Altmann, H.; Kluger, F.; Stamatelopoulos, G.-N. *Energy Procedia* **2009**, *1* (1), 581−589.

(10) Edge, P.; Gharebaghi, M.; Irons, R.; Porter, R.; Porter, R. T. J.; Pourkashanian, M.; Smith, D.; Stephenson, P.; Williams, A. *Chem. Eng. Res. Des.* **2011**, *89* (9), 1470−1493.

(11) Launder, B. E.; Spalding, D. B. *Lectures in Mathematical Models of Turbulence*; Academic Press: London, England, 1972.

(12) Orszag, S. A. Y.; Yakhot, V.; Flannery, W. S.; Boysan, F.; Choudhury, D.; Maruzewski, J.; Patel, B., Renormalization Group Modeling and Turbulence Simulations. In *International Conference on Near-Wall Turbulent Flows*, Tempe, Arizona, 1993.

(13) Wilcox, D. C. *Turbulence modeling for CFD*; DCW Industries, Inc.: La Cãnada, CA, 1993; p xix, 460 p.

(14) Menter, F. R. *AIAA J.* **1994**, *32* (8), 1598−1605.

(15) Khare, S. P.; Wall, T. F.; Farida, A. Z.; Liu, Y.; Moghtaderi, B.; Gupta, R. P. *Fuel* **2008**, *87* (7), 1042−1049.

(16) Nozaki, T.; Takano, S.-i.; Kiga, T.; Omata, K.; Kimura, N. *Energy* **1997**, *22* (2−3), 199−205.

(17) Chui, E. H.; Majeski, A. J.; Douglas, M. A.; Tan, Y.; Thambimuthu, K. V. *Energy* **2004**, *29* (9−10), 1285−1296.

(18) Rehfeldt, S.; Kuhr, C.; Ehmann, M.; Bergins, C.; Scheffknecht, G.; Maier, J.; Wu, S. Basic experiments and CFD calculations of air and oxyfuel firing of lignite and bituminous coals in 0.5 and 1 MW scale combustion test facilities. In *The 34th International Technical Conference on Clean Coal and Fuel Systems*, Clearwater, FL, 2009.

(19) Toporov, D.; Bocian, P.; Heil, P.; Kellermann, A.; Stadler, H.; Tschunko, S.; Forster, M.; Kneer, R. *Combust. Flame* **2008**, *155* (4), 605−618.

(20) Muller, M.; Lemp, O.; Leiser, S.; Schnell, U.; Grathwohl, S.; Maier, J.; Scheffknecht, G.; Kluger, F.; Monckert, P. Advanced modeling of pulverized coal combustion under oxy-fuel conditions. In *The 35th International Technical Conference on Clean Coal and Fuel Systems*, Clearwater, FL, 2010.

(21) Nikolopoulos, N.; Nikolopoulos, A.; Karampinis, E.; Grammelis, P.; Kakaras, E. *Fuel* **2011**, *90* (1), 198−214.

(22) Al-Abbas, A. H.; Naser, J.; Dodds, D. *Fuel* **2011**, *90* (5), 1778−1795.

(23) Pope, S. B. *Turbulent flows*; Cambridge University Press: Cambridge, New York, 2000; p xxxiv, 771 p.

(24) Kumar, M.; Ghoniem, A. F. *Energy Fuels* **2011**, *26* (1), 451−463.

(25) Kumar, M.; Ghoniem, A. F. *Energy Fuels* **2011**, *26* (1), 464−479.

(26) Edge, P.; Gubba, S. R.; Ma, L.; Porter, R.; Pourkashanian, M.; Williams, A. *Proc. Combustion Inst.* **2011**, *33* (2), 2709−2716.

(27) Gharebaghi, M.; Irons, R. M. A.; Ma, L.; Pourkashanian, M.; Pranzitelli, A. *Int. J. Greenhouse Gas Control* **2011**, *5* (Supplement1, (0)), S100−S110.

(28) Heil, P.; Toporov, D.; Stadler, H.; Tschunko, S.; Forster, M.; Kneer, R. *Fuel* **2009**, *88* (7), 1269−1274.

(29) Beer, J. M.; Chigier, N. A. *Combustion aerodynamics*; Krieger: Malabar, FL, 1983; p x, 264 p.

(30) ANSYS FLUENT 12.0 Theory Guide. In 2009.

(31) Smagorinsky, J. *Mon. Weather Rev.* **1963**, *91* (3), 99−164.

(32) Migdal, D.; Agosta, V. D. American Society of Mechanical, E. *A source flow model for continuum gas-particle flow*; ASME: New York, NY, 1967.

(33) Badzioch, S.; Hawksley, P. G. W. *Ind. Eng. Chem. Process Des. Dev.* **1970**, *9* (4), 521−530.

(34) Bejarano, P. A.; Levendis, Y. A. *Combust. Flame* **2008**, *153* (1−2), 270−287.

(35) Shaddix, C. R.; Molina, A. *Proc. Combust. Inst.* **2009**, *32* (2), 2091−2098.

(36) Shaddix, C. R.; Hecht, E. S.; Geier, M.; Molina, A.; Haynes, B. S. Effect of gasification reactions on oxy-fuel combustion of pulverized coal char. In *The 35th International Technical Conference on Clean Coal & Fuel Systems*, Clearwater, FL, 2010.

(37) Hecht, E. S.; Shaddix, C. R.; Molina, A.; Haynes, B. S. *Proc. Combust. Inst.* **2011**, *33* (2), 1699−1706.

(38) Mitchell, R. E.; Kee, R. J.; Glarborg, P.; Coltrin, M. E. *Symp. (Int.) Combust., [Proc.]* **1991**, *23* (1), 1169−1176.

(39) Tognotti, L.; Longwell, J. P.; Sarofim, A. F. *Symp. (Int.) Combust., [Proc.]* **1991**, *23* (1), 1207−1213.

(40) Wall, T.; Rhelan, W.; Bartz, S. Doc. F388/a/3; International Flame Research Foundation: Livorno, Italy, 1976.

(41) Brown, B. W.; Smoot, L. D.; Smith, P. J.; Hedman, P. O. *AIChE J.* **1988**, *34* (3), 435−446.

(42) Smith, I. W. *Symp. (Int.) Combust., [Proc.]* **1982**, *19* (1), 1045−1065.

(43) Magnussen, B. F.; Hjertager, B. H. *Symp. (Int.) Combust., [Proc.]* **1977**, *16* (1), 719−729.

(44) Spalding, D. B. *Symp. (Int.) Combust., [Proc.]* **1971**, *13* (1), 649−657.

(45) Glarborg, P.; Bentzen, L. L. B. *Energy Fuels* **2008**, *22* (1), 291−296.

(46) Andersen, J.; Rasmussen, C. L.; Giselsson, T.; Glarborg, P. *Energy Fuels* **2009**, *23* (3), 1379−1389.

(47) Porter, R.; Liu, F.; Pourkashanian, M.; Williams, A.; Smith, D. *J. Quant Spectrosc. Radiat. Transfer* **2010**, *111* (14), 2084−2094.

(48) Raithby, G. D.; Chui, E. H. *J. Heat Transfer* **1990**, *112* (2), 415−423.

(49) Chui, E. H.; Raithby, G. D. *Numer. Heat Transfer, Part B* **1993**, *23* (3), 269−288.

(50) Hottel, H. C.; Sarofim, A. F. *Radiative transfer*; McGraw-Hill: New York, 1967; p xxiv, 520 p.

(51) Smith, T. F.; Shen, Z. F.; Friedman, J. N. *ASME J. Heat Transfer* **1982**, *104*, 602−608.

(52) Johansson, R.; Andersson, K.; Leckner, B.; Thunman, H. *Int. J. Heat Mass Transfer* **2010**, *53* (1−3), 220−230.

(53) Kangwanpongpan, T.; Corrêa da Silva, R.; Krautz, H. J. *Energy* **2012**, *41* (1), 244−251.

(54) Kimura, N.; Omata, K.; Kiga, T.; Takano, S.; Shikisima, S. *Energy Convers. Manage.* **1995**, *36* (6−9), 805−808.

(55) Hjartstam, S.; Andersson, K.; Johnsson, F.; Leckner, B. *Fuel* **2009**, *88* (11), 2216−2224.

(56) Zhang, J.; Kelly, K. E.; Eddings, E. G.; Wendt, J. O. L. *Proc. Combust. Institute* **2011**, *33* (2), 3375−3382.

(57) Fry, A.; Adams, B.; Shan, J. Oxy-burner retrofit principles for existing coal-fired utility boilers. In *The 35th International Technical Conference on Clean Coal & Fuel Systems*, Clearwater, FL, 2010.

(58) Field, M. A. *Combust. Flame* **1969**, *13* (3), 237−252.

■ NOTE ADDED AFTER ASAP PUBLICATION

This paper originally published July 12, 2012. Reference 53 was updated with publication information and the article reposted on July 20, 2012.